

Integrated feature scale modeling of plasma processing of porous and solid SiO₂. I. Fluorocarbon etching

Arvind Sankaran^{a)}

Department of Chemical and Biomolecular Engineering, University of Illinois, 1406 W. Green St., Urbana, Illinois 61801

Mark J. Kushner^{b)}

Department of Electrical and Computer Engineering, University of Illinois, 1406 W. Green St., Urbana, Illinois 61801

(Received 15 January 2004; accepted 3 May 2004; published 14 July 2004)

Increases in RC delay times in interconnect wiring for microelectronics as feature sizes decrease have motivated investigations into the use of low-dielectric constant insulators, and in particular, porous silicon-dioxide (PS). Profile evolution and maintenance of critical dimensions during plasma etching of PS are problematic due to the exposure of open pores. To investigate these issues, reaction mechanisms for fluorocarbon plasma etching of SiO₂ in C₂F₆, CHF₃, and C₄F₈ chemistries have been developed and incorporated into the Monte Carlo Feature Profile Model which was modified to address these two-phase systems. The reaction mechanism was validated by comparison to experiments by others for etching of PS and solid SiO₂ (SS). We found that the etch rates for PS are generally higher than that of SS due to the inherently lower mass fraction. Mass corrected etch rates of PS can be larger or smaller than those for SS depending on the degree of pore filling by polymer and the degree of ion activated chemical sputtering. Pore filling is particularly important for PS having open networks with large pores and high porosities. We found little dependence of the taper of high aspect ratio profiles on the average pore radius and porosity. However, the profile changes from tapered to bowed as the interconnectivity of the porous network increases. Scaling laws for profile shapes are otherwise similar for both SS and PS. © 2004 American Vacuum Society. [DOI: 10.1116/1.1764821]

I. INTRODUCTION

The increase in the area density of devices and the reduction of the size of devices in microelectronics have resulted in the potential for increasing the RC delay time in interconnect wiring.¹ Low dielectric constant (low-*k*) materials are being investigated as the inter-level dielectrics in interconnect wiring to reduce this delay. Low-*k* dielectrics can be broadly classified as organic and inorganic.² Organic materials such as polytetrafluoroethylene (PTFE) and parylene are etched in oxygen based plasmas (O₂-Ar and O₂-N₂).³⁻⁵ Inorganic dielectrics typically involve SiO₂ based materials which are etched in fluorocarbon plasmas.^{6,7} Porous SiO₂ (PS) is one such inorganic low-*k* material. Successful integration of PS films as an inter-level dielectric depends on its electrical, thermo-mechanical, chemical and structural properties. Of interest in this work are their structural properties, which are porosity, average pore radius and pore interconnectivity.⁸

Measurements of PS characteristics using small angle x-ray spectroscopy combined with x-ray reflectivity and ellipsometric porosimetry indicate that the typical porosities used for interlevel dielectrics are 20%–80%.^{9,10} The dielectric constant is generally reduced in proportion to the mass

density, which is inversely proportional to the porosity. PS with an interconnected pore structure typically experiences an increase in dielectric constant during processing due to a partial collapse of the pore structure.⁹ The connectivity of pores in industrially relevant materials can be large. For example, Wu *et al.* utilized small angle neutron spectroscopy to determine that 22% of the pores of a 900 nm thick PS thin film (AlliedSignal Nanoglass™ K2.2-A10B) have connective paths to the free surface.⁹ Gidley *et al.* measured 100% pore interconnectivity in a methylsilsesquioxane (MSQ) film (*k*=2.5) using positron annihilation lifetime spectroscopy.¹¹ Pore measurements using these techniques predict typical radii to 2–20 nm.^{9,12}

Standaert *et al.* have investigated fluorocarbon etching of fluorinated SiO₂, hydrogen silsesquioxane (HSQ) and MSQ films using an inductively coupled plasma system.¹³ Comparisons were made to the etching of solid SiO₂ (SS) in CHF₃ and C₄F₈ chemistries. The etch rate of PS was in general higher than that of SS due to the lower mass densities of PS. However in highly polymerizing environments they found that the etch rate of PS was suppressed compared to SS. They also investigated profile evolution of HSQ and MSQ etched in a CHF₃ plasma and found similar scaling laws as for SS.^{2,13}

Fluorocarbon etching of both PS and SS proceeds through the formation of an overlying fluorocarbon polymer on the SiO₂.¹⁴ C_xF_y radicals are the precursors to the polymer layer which regulates the delivery of activation energy and the

^{a)}Present address: Novellus Systems, 11155 SW Leveton Dr., Tualatin, OR 97062; electronic mail: arvind.sankaran@novellus.com

^{b)}Author to whom correspondence should be addressed; electronic mail: mjk@uiuc.edu

transport of neutral and ion fluxes to the underlying materials.¹⁵ Upon delivery of activation energy to the polymer–SiO₂ interface the oxygen in SiO₂ reacts with the fluorocarbon species in the polymer to release etch products such as COF_x, thereby consuming the polymer.¹⁶ This leads to a thinner polymer layer during SiO₂ etching compared to Si etching.¹⁷ The thickness of the polymer layer is the primary source of selectivity between different materials such as SiO₂, Si₃N₄, and Si as the etch rate generally scales inversely with the polymer thickness.¹⁸ Polymer is also consumed by energetic ion sputtering.^{19,20}

In this work, predictions for the etching of PS in fluorocarbon plasmas will be discussed using results from a two-phase algorithm incorporated into the Monte Carlo Feature Profile Model (MCFPM).^{21,22} The MCFPM was integrated with the Hybrid Plasma Equipment Model (HPEM), which provides the energy and angular distributions of the neutral and charged species incident on the wafer surface.^{23,24} A surface reaction mechanism first discussed in Ref. 22, was generalized and improved to be applicable to CHF₃, C₂F₆, and C₄F₈ chemistries. The logic is that a surface reaction mechanism should depend only on the fundamental processes and not on either the magnitude or the sources of the reactants. Therefore, if correct, a reaction mechanism should apply to any fluorocarbon system. To this end, the model was compared to experiments for CHF₃, C₂F₆ and C₄F₈ chemistries for both PS and SS, and good agreement was obtained.^{25,26} These results form the basis of an investigation of cleaning of polymer from PS using oxygen plasmas, and deposition of barrier coatings onto PS discussed in the companion paper, Part II.²⁷

We found that the etch rate of SS increases as a function of self-bias after a threshold, and saturates at high biases. Etching of PS follows similar trends as SS with etch rates in general being higher due to the inherent lower mass densities of PS. However, the mass corrected etch rates of PS depend on the filling of pores by polymer, which can either enhance or reduce the etch rates. Pore filling is most significant for interconnected porous networks having large pores and high porosities. Profiles become less tapered with increasing bias and decreasing polymerizing fluxes. The taper of profiles has little dependence on the pore radius and porosity, however, open pore networks tend to produce bowed profiles.

The HPEM, the MCFPM, and the two-phase algorithm for PS will be discussed in Sec. II. The surface reaction mechanism for fluorocarbon etching of SiO₂ and Si will be discussed in Sec. III. Validation of the surface reaction mechanism and the two-phase model will be presented in Secs. IV and V. Results from the MCFPM for etching of PS and SS in high aspect ratio trenches will be discussed in Sec. VI followed by concluding remarks in Sec. VII.

II. DESCRIPTION OF THE MODELS

A. Reactor scale models

The HPEM used to obtain reactant fluxes to the substrate has been previously described and so will only be summarized here.^{24,28} The HPEM is a two-dimensional simulator

which addresses equipment scale plasma chemistry and hydrodynamics, and consists of the Electromagnetics Module, the Electron Energy Transport Module, and the Fluid Kinetics Module. Electromagnetic and magneto-static fields are calculated in the Electromagnetics Module. These fields are then used in the Electron Energy Transport Module to obtain electron impact source functions and transport coefficients. This is achieved by either solving the electron energy equation or by a Monte Carlo simulation. These results are then passed to the Fluid Kinetics Module, in which separate continuity, momentum and energy equations are solved for ions and neutral species. A drift diffusion formulation is used for electrons to enable an implicit solution of the Poisson's equation for the time varying electrostatic potential. Output from the Fluid Kinetics Module (densities and electrostatic fields) is then transferred to the other modules. This process is iterated until a converged solution is obtained.

The Plasma Chemistry Monte Carlo Module (PCMCM) in the HPEM produces the energy and angular distributions for neutrals and ions striking the wafer surface.²⁴ The PCMCM launches pseudoparticles representing ions and neutrals based on the electron impact source functions and the time dependent electric fields obtained from the other modules of the HPEM. Using a Monte Carlo simulation, the PCMCM tracks the trajectories of the ions and neutrals while capturing their gas phase collisions and interactions with the surface using the same reaction mechanism as in the HPEM. Statistics are collected on the energy and angle of pseudoparticles as they strike specified locations on surfaces to produce time-averaged energy and angular distributions. The MCFPM then uses these distributions at the wafer to predict etch profiles.

B. Feature scale model

The two-dimensional MCFPM has been previously described and so will be briefly summarized here.^{21,22,29,30} The fluxes of reactant species and their energy and angular distributions from the HPEM are inputs to the MCFPM. The MCFPM resolves the surface (mask, photoresists, semiconductors) using a two-dimensional (2D) rectilinear mesh. Each cell in the mesh has a material identity. Pseudoparticles representing the incident plasma species are randomly selected from the energy and angular distributions obtained from the PCMCM and launched towards the surface. A generalized surface reaction mechanism controls the interaction between the gas-phase pseudoparticles and the computational mesh cells which represent the surface. The reaction mechanism is ultimately expressed as a probability array encompassing all possible reactions between the pseudoparticle plasma species and the surface species. When a pseudoparticle strikes a given material cell, a reaction is chosen based on these probability arrays using Monte Carlo techniques. Based on the selected reaction, the identities of the mesh cells change representing reaction products. Material is added representing deposition or removed constituting an etch product. Gas-phase species evolving from these reactions are tracked as new gas-phase pseudoparticles. The

mesh used to resolve our features consisted of square cells having dimensions of 1.5 nm or approximately ≈ 4 atomic spacings.

The specifics of the interaction of energetic particles with surface species are determined by their energy and angular distributions. The source of energetic particles is ions accelerated through the sheath, with energies of up to 100s eV and angular spreads $< 5^\circ - 10^\circ$ from the vertical. We assumed that ions neutralize upon interaction with the surface and so do not distinguish between energetic ions and energetic neutrals. Energetic particles can either specularly or diffusively reflect from surfaces, with an energy loss which is larger for diffusive scattering and smaller for specular scattering.

Following the work of Barklund and Blom³¹ and Schaepekens *et al.*³² our generalized reaction probability for a particle of energy E incident onto a surface at an angle θ from the local vertical of the surface is

$$p(\theta) = p_0 \left[\frac{E^n - E_t^n}{E_r^n - E_t^n} \right] f(\theta), \quad (1)$$

where E_t is the threshold energy of the process, E_r is a reference energy, p_0 is the probability for normal incidence at E_r and $f(\theta)$ is the relative probability at angle of incidence θ . Based on the work of Schaepekens *et al.* $f(\theta)$ is an empirical function typical of chemically enhanced sputtering with a mild maximum value near $\theta = 60^\circ$.³⁰ It should be noted that there are differing results in the literature for the angular dependence of the yield of SiO₂ etching in fluorocarbon plasmas which are likely a result of process conditions. For example, in the work of Schaepekens *et al.* there is a maximum in the etch yield of SiO₂ in CHF₃ and C₃F₆ plasmas at 55° compared to 0°. In more recent work by Chae, Vitale, and Sawin³³ the etch yield of SiO₂ in C₂F₆ and C₄F₈ plasmas peaked at normal incidence. In mixtures with O₂, where the polymer is thinner, the yield was less peaked at normal incidence. This effect is particularly pronounced in the etching of Si₃N₄ etching where the angular dependence of the yield in a CHF₃-O₂ chemistry depends on gas pressure and oxygen fraction, an effect attributed to the thickness of the polymer.³¹ For low polymerizing conditions, the yield was peaked at 60 degrees commensurate physio-chemical sputtering. For highly polymerizing conditions, the yield was maximum at normal incidence, an effect in part attributed to the smaller delivery of activation energy through the polymer to the polymer-substrate interface.

In our model, the etch probability is directly determined by the delivery of activation energy to the polymer-substrate interface, and so the less normal peaked angular dependence seems appropriate. For example, in our surface site balance model²² the energy of ions is degraded based on the thickness of the overlying polymer. The issue of the angular dependence of the etch yield as a function of polymer thickness is particularly important in a system where the polymer thickness has a wide variation, as in polymer filling of pores. Future improvements to the model will address these points in more detail.

The reflection of particles from surfaces was given both specular and diffusive character. To account for surface roughness on spatial scales not resolved by our model, we specified that a fraction $f_d = 0.25$ was diffusively scattered. The energy of specularly reflected particle was scaled such that forward scattered particles retain the majority of their energy. The specularly reflected particle energy for incident energy E_I is

$$E_s(\theta) = E_I \left(\frac{E_I - E_c}{E_{ts} - E_c} \right) \left(\frac{\theta - \theta_c}{90^\circ - \theta_c} \right), \quad (2)$$

for $\theta > \theta_c$, $E_c < E_I < E_{ts}$. Particles having $\theta < \theta_c$ or $E_I < E_c$ are said to diffusively scatter. Particles having $E_I > E_{ts}$ are said to retain all of their energy subject to the angular correction. We used $E_{ts} = 100$ eV, $E_c = 0$ eV, and $\theta_c = 60^\circ$. The final reflected energy of the particle is a weighted sum of the specularly reflected energy and diffusively reflected energy.

The construction of the probability arrays for interaction of gas phase with surface cells is problematic due to the energy dependence of the reaction probability and the requirement that probabilities add to unity for the interaction of any gas-phase species with the surface. This process is facilitated by use of a null process for all combinations of incident gas-phase species and surface species. The null process is reflection without reaction. As the probability of energy dependent processes change, the null portion of the probability array is rescaled to ensure that the sum of probabilities is unity. Should an etch yield exceed unity, the null reaction is eliminated and the array is rescaled.

PS is modeled as being stoichiometric SiO₂ with vacuum pores. In this two-dimensional model, the pores can at best be represented as cylinders. The pore radii and locations are randomly chosen and distributed in the numerical mesh used by the MCFPM with a Gaussian distribution of radii having probability

$$p(r) \sim \exp(-((r - r_0)/\Delta r)^2), \quad (3)$$

where r is the radius of the incorporated pore, r_0 is the average pore radius, and Δr is the standard deviation. (Pore size in subsequent discussion refers to r_0 .) The numerical mesh we used for the majority of the studies presented here had a cell size 1.5 nm. The lower limit of our resolution is 4 nm diameter pore. We performed sensitivity studies on the size of the mesh and are confident that our conclusions are not being biased by our mesh size.

Algorithms were developed to include the capability of creating both closed and interconnected pore networks. The interconnectivity of the network is the fraction of pores that are connected to another pore. PS having an interconnectivity of 0% consists of isolated pores. In PS having an interconnectivity of 100% every pore is connected to at least one other pore in a low fractal dimension manner. To create an interconnected structure, the following procedure is used. Based on the specified fractional interconnectivity, a pore is randomly chosen to be isolated or connected. Pore locations and radii are then also randomly chosen. As pores are created in the mesh, the numerical cells which are on the inside of

pores are tracked. Pores which overlap result in some fraction of the mesh cells being owned by both pores. For an isolated pore, mesh cells can be owned by only a single pore. For an interconnected pore at most two pores can own any given mesh cell. If a randomly placed pore overlaps a cell which is already owned by the maximum allowed pores, the placement is disallowed. The end result is that the pores are chainlike with a low fractal dimension. Higher fractal dimensions can be obtained by allowing ownership of a cell by additional pores. The pore placement process is repeated until the desired porosity is achieved.

As etching proceeds, computationally solid mesh cells may become isolated from the remainder of the mesh. For nonporous single-phase materials, such cells are dropped or are moved vertically to rejoin a solid surface. This is a more difficult challenge when modeling PS, in that the unopened vacuum pores must be differentiated from the bulk. During pore creation, the maximum pore dimension in each column of the mesh is stored. As the etch evolves, a solid mesh cell is treated as being isolated if its vertical distance to the closest surface is greater than the maximum pore size in that column. At such time, the isolated solid mesh cell is transitioned to a surface.

III. SURFACE REACTION MECHANISMS FOR FLUOROCARBON PLASMA ETCHING OF SiO_2 AND Si

A. Basic mechanism

Surface reaction mechanisms, in general, are an intrinsic property of the gas-phase reactant species (incident on the surface) and the surface. As such reaction mechanisms should be independent of the process conditions, such as the plasma source or the gas chemistry. The process conditions may determine the energies and magnitudes of the incident reactant fluxes, however the reaction mechanism should not change. We have attempted to address this issue by developing a generalized reaction mechanism applicable to etching of SiO_2 in at least three different fluorocarbon chemistries which initially consists of the feedstock gases of C_2F_6 , CHF_3 , or C_4F_8 .

The reaction mechanism for etching of SiO_2 and Si in fluorocarbon plasmas is schematically shown in Fig. 1 and is listed in Table I. The fluxes to the substrate consist of polymerizing neutral radicals, energetic ionic species and neutral etching radicals. The polymerizing radicals are C_xF_y where there are at least two unpaired electrons. The reaction proceeds by the formation of a steady-state polymer layer on top of the substrate.^{16,34} The initial layer of polymer on SiO_2 forms a $\text{SiO}_2\text{C}_x\text{F}_y$ complex, which is the precursor to etching. Further polymer growth is problematic as polymerizing radicals are thought to have little probability of sticking to the $\text{SiO}_2\text{C}_x\text{F}_y$ complex. In this regard, it has been proposed that low energy ion bombardment promotes the formation of polymer by activating surface sites.^{34–37} For example, Goto *et al.* investigated polymer growth using a CF_2 beam in an Ar microwave plasma with Ar^+ energies in the low 10's eV.³⁵ They found that polymer deposition was significantly

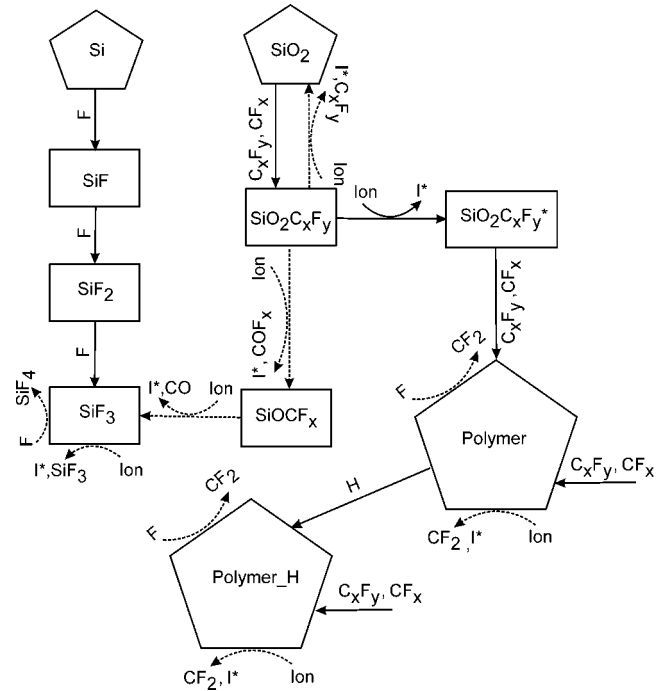


Fig. 1. Schematic of surface reaction mechanism for fluorocarbon etching of SiO_2 and Si. Bulk surface species are represented by pentagons. Intermediate complexes are represented by rectangles. The remaining are gas phase species. I^* refers to a hot neutral. Solid arrows represent deposition reactions and dotted arrows represent etching reactions.

higher in the presence of Ar^+ than when only a CF_2 beam was used. Similarly, Booth *et al.* observed a high CF_2 sticking rate in low power rf discharges.³⁶

To address this activation process, polymer deposition on the $\text{SiO}_2\text{C}_x\text{F}_y$ complex is modeled by a two step process. The $\text{SiO}_2\text{C}_x\text{F}_y$ complex sites in the presence of low energy ion bombardment are activated to form the intermediate $\text{SiO}_2\text{C}_x\text{F}_y^*$. The probability of activation of the $\text{SiO}_2\text{C}_x\text{F}_y$ sites for incident energy E_i scales as

$$p(E_i) = p_0 \times \max\left(0, 1 - \frac{E_i}{E_c}\right), \quad (4)$$

where E_c is the maximum energy of the process, and p_0 is the probability at zero incident energy. CF_x and C_xF_y radicals have a higher sticking probability to the activated sites and thus forms the first layer of the polymer. Subsequent polymer growth can occur on top of this first layer.

Once the substrate is covered with a monolayer of polymer, the incoming radicals and ions do not see the underlying substrate and hence the growth in polymer must be independent of the underlying substrate. However Schaepekens *et al.* observed that prior to saturation the polymer layer is thinner on SiO_2 than on Si.²⁶ This suggested polymer consumption processes at the SiO_2 -polymer interface. The oxygen atoms in SiO_2 can react with the carbon and fluorine in the polymer network to consume polymer and simultaneously release etch products like CO_x , COF_x . Oehrlein *et al.* observed that the SiO_2 and Si etch rates in general decrease with increasing polymer layer thickness, which scales inversely with

TABLE I. Surface reaction mechanism.

Species					Symbol
Ions					CF_3^+
Polymerizing radicals					CF_x, C_xF_y
Fluorocarbon polymer					P
Hydrogenated polymer					HP
Activated species					*
Gas phase species					g
Hot neutrals					h
Surface species					s
Reaction ^{a,b}					Reference
Formation of complex at polymer-SiO ₂ interface:					
$SiO_{2s} + CF_{xg} \rightarrow SiO_2CF_{xs}$	p_0				
$SiO_{2s} + C_xF_{yg} \rightarrow SiO_2C_xF_{ys}$	0.1				
Low energy Ion activation to form activated complex site					
$SiO_2CF_s + CF_{3g}^+ \rightarrow SiO_2CF_s^* + CF_{3h}$	p_0	E_c (eV)			
$SiO_2CF_{2s} + CF_{3g}^+ \rightarrow SiO_2CF_{2s}^* + CF_{3h}$	0.1	70			Eq. (4)
$SiO_2C_2F_{3s} + CF_{3g}^+ \rightarrow SiO_2C_2F_{3s}^* + CF_{3h}$	0.1	70			Eq. (4)
$SiO_2C_2F_{4s} + CF_{3g}^+ \rightarrow SiO_2C_2F_{4s}^* + CF_{3h}$	0.1	70			Eq. (4)
$SiO_2CF_s + CF_{3g}^+ \rightarrow SiO_2CF_s + P_s$	0.1	70			Eq. (4)
$SiO_2CF_{2s} + CF_{3g}^+ \rightarrow SiO_2CF_{2s} + P_s$	0.1	70			Eq. (4)
$SiO_2C_2F_{3s} + CF_{3g}^+ \rightarrow SiO_2C_2F_{3s} + P_s$	0.1	70			Eq. (4)
$SiO_2C_2F_{4s} + CF_{3g}^+ \rightarrow SiO_2C_2F_{4s} + P_s$	0.1	70			Eq. (4)
Ion activated dissociation of complex					
$SiO_2CF_s + CF_{3g}^+ \rightarrow SiO_{2s} + CF_g + CF_{3h}$	p_0	E_{th} (eV)	E_r (eV)	n	
$SiO_2CF_{2s} + CF_{3g}^+ \rightarrow SiO_{2s} + CF_{2g} + CF_{3h}$	0.08	70	140	0.97	Eq. (1)
$SiO_2C_2F_{3s} + CF_{3g}^+ \rightarrow SiOCF_{3s} + CO_g + CF_{3h}$	0.08	70	140	0.97	Eq. (1)
$SiO_2C_2F_{3s} + CF_{3g}^+ \rightarrow SiO_{2s} + C_2F_{3g} + CF_{3h}$	0.90	70	140	0.97	Eq. (1)
$SiO_2C_2F_{4s} + CF_{3g}^+ \rightarrow SiOCF_{4s} + CO_g + CF_{3h}$	0.03	70	140	0.97	Eq. (1)
$SiO_2C_2F_{4s} + CF_{3g}^+ \rightarrow SiO_{2s} + C_2F_{4g} + CF_{3h}$	0.90	70	140	0.97	Eq. (1)
$SiOCF_{3s} + CF_{3g}^+ \rightarrow SiF_{2s} + COF_g + CF_{3h}$	0.03	70	140	0.97	Eq. (1)
$SiOCF_{4s} + CF_{3g}^+ \rightarrow SiF_{3s} + COF_g + CF_{3h}$	0.01	70	140	0.97	Eq. (1)
$SiOCF_{4s} + CF_{3g}^+ \rightarrow SiF_{3s} + COF_g + CF_{3h}$	0.01	70	140	0.97	Eq. (1)
$SiO_2CF_s^* + CF_{3g}^+ \rightarrow SiO_{2s} + CF_g + CF_{3h}$	0.08	70	140	0.97	Eq. (1)
$SiO_2CF_{2s}^* + CF_{3g}^+ \rightarrow SiO_{2s} + CF_{2g} + CF_{3h}$	0.08	70	140	0.97	Eq. (1)
$SiO_2C_2F_{3s}^* + CF_{3g}^+ \rightarrow SiOCF_{3s} + CO_g + CF_{3h}$	0.90	70	140	0.97	Eq. (1)
$SiO_2C_2F_{3s}^* + CF_{3g}^+ \rightarrow SiO_{2s} + C_2F_{3g} + CF_{3h}$	0.03	70	140	0.97	Eq. (1)
$SiO_2C_2F_{4s}^* + CF_{3g}^+ \rightarrow SiOCF_{4s} + CO_g + CF_{3h}$	0.90	70	140	0.97	Eq. (1)
$SiO_2C_2F_{4s}^* + CF_{3g}^+ \rightarrow SiO_{2s} + C_2F_{4g} + CF_{3h}$	0.03	70	140	0.97	Eq. (1)
$SiOCF_{3s}^* + CF_{3g}^+ \rightarrow SiF_{2s} + COF_g + CF_{3h}$	0.01	70	140	0.97	Eq. (1)
$SiOCF_{4s}^* + CF_{3g}^+ \rightarrow SiF_{3s} + COF_g + CF_{3h}$	0.01	70	140	0.97	Eq. (1)
$SiF_{3s}^* + CF_{3g}^+ \rightarrow SiF_{3g} + CF_{3h}$	0.99	70	140	0.97	Eq. (1)
Reactions with polymerizing species					
$SiO_2CF_s + CF_{xg} \rightarrow SiO_2C_2F_{3s}$	p_0				
$SiO_2CF_{2s} + CF_{xg} \rightarrow SiO_2C_2F_{4s}$	0.10				
$SiO_2CF_s^* + CF_{xg} \rightarrow SiO_2CF_s + P_s$	0.10				
$SiO_2CF_{2s}^* + CF_{xg} \rightarrow SiO_2CF_{2s} + P_s$	0.5				
$SiO_2C_2F_{3s}^* + CF_{xg} \rightarrow SiO_2C_2F_{3s} + P_s$	0.5				
$SiO_2C_2F_{4s}^* + CF_{xg} \rightarrow SiO_2C_2F_{4s} + P_s$	0.5				
$SiO_2CF_s^* + C_xF_{yg} \rightarrow SiO_2CF_s + P_s$	0.5				
$SiO_2CF_{2s}^* + C_xF_{yg} \rightarrow SiO_2CF_{2s} + P_s$	0.5				
$SiO_2C_2F_{3s}^* + C_xF_{yg} \rightarrow SiO_2C_2F_{3s} + P_s$	0.5				
$SiO_2C_2F_{4s}^* + C_xF_{yg} \rightarrow SiO_2C_2F_{4s} + P_s$	0.5				
$Si_s + CF_{xg} \rightarrow Si_s + P_s$	0.15				
$Si_s + C_xF_{yg} \rightarrow Si_s + P_s$	0.15				
$SiF_s + CF_{xg} \rightarrow SiF_s + P_s$	0.15				
$SiF_{2s} + CF_{xg} \rightarrow SiF_{2s} + P_s$	0.15				
$SiF_s + C_xF_{yg} \rightarrow SiF_s + P_s$	0.15				
$SiF_{2s} + C_xF_{yg} \rightarrow SiF_{2s} + P_s$	0.15				
$SiF_{3s} + CF_{xg} \rightarrow SiF_{3s} + P_s$	0.15				
$SiF_{3s} + C_xF_{yg} \rightarrow SiF_{3s} + P_s$	0.15				
Fluorination					
$Si_s + F_g \rightarrow SiF_s$	p_0				
	0.05				

TABLE I. (Continued).

Reaction ^{a,b}					Reference
$\text{SiF}_s + \text{F}_g \rightarrow \text{SiF}_{2s}$	0.05				
$\text{SiF}_{2s} + \text{F}_g \rightarrow \text{SiF}_{3s}$	0.05				
$\text{SiF}_{3s} + \text{F}_g \rightarrow \text{SiF}_{4g}$	0.10				
$\text{SiO}_2\text{CF}_x + \text{F}_g \rightarrow \text{SiF}_{2s} + \text{CO}_{2g}$	0.01				
$\text{SiO}_2\text{CF}_{2s} + \text{F}_g \rightarrow \text{SiF}_{3s} + \text{CO}_{2g}$	0.01				
Reactions on polymer surface	p_0	$E_{th}(\text{eV})$	$E_r(\text{eV})$	n	
$\text{P}_s + \text{F}_g \rightarrow \text{CF}_{2g}$	0.03				
$\text{P}_s + \text{H}_g \rightarrow \text{P}_s + \text{HP}_s$	0.90				
$\text{P}_s + \text{C}_x\text{F}_y\text{g} \rightarrow \text{P}_s + \text{P}_s$	0.15				
$\text{P}_s + \text{CF}_{xg} \rightarrow \text{P}_s + \text{P}_s$	0.15				
$\text{P}_s + \text{CF}_{3g}^+ \rightarrow \text{CF}_{3h} + \text{CF}_{2g}$	0.15	70	140	0.97	Eq. (1)
$\text{HP}_s + \text{F}_g \rightarrow \text{CF}_{2g}$	0.03				
$\text{HP}_s + \text{H}_g \rightarrow \text{HP}_s + \text{HP}_s$	0.99				
$\text{HP}_s + \text{C}_x\text{F}_y\text{g} \rightarrow \text{HP}_s + \text{HP}_s$	0.05				
$\text{HP}_s + \text{CF}_{xg} \rightarrow \text{HP}_s + \text{HP}_s$	0.05				
$\text{HP}_s + \text{CF}_{3g}^+ \rightarrow \text{CF}_{3h} + \text{CF}_{2g}$	0.28	125	175	0.98	Eq. (1)

^aReactions for CF_{3g}^+ are generic for all ions. All ions return from surfaces as hot neutrals. Ions and hot neutrals have the same mechanism.

^bIn reactions with no chemical change, the gas species are reflected of the surface. These reactions are not shown in the table.

bias.^{17,18,26} This suggested that the polymer consumption process at the interface increased at higher substrate biases and is enhanced by energetic ions. This process is modeled as a chemically enhanced sputtering process, with an energy dependence following Eq. (1). The $\text{SiO}_2\text{C}_x\text{F}_y$ complex formed at the polymer–wafer interface undergoes chemically enhanced sputtering and dissociates into SiOCF_y and releases COF_x as etch products. SiOCF_y in turn undergoes chemically enhanced sputtering to dissociate to SiF_3 and releases CO_x as etch products. SiF_3 is finally sputtered to etch away the wafer and in the process release SiF_3 as etch product. SiF_3 is also consumed by F atom etching to release SiF_4 .

Polymer formation and consumption processes occur simultaneously producing a steady-state polymer layer thickness. The important polymer consumption processes are physical sputtering and F atom etching. Similar to chemically enhanced sputtering, physical sputtering of the polymer layer increases with ion energy as in Eq. (1). In the case of F atom etching, F radicals terminate the dangling bonds of carbon in the polymer chains to release volatile etch products such as CF_4 . For fluorocarbon gas chemistries with H in the gas phase, such as CHF_3 , the H radicals can stick to the fluorocarbon polymer network as side chains and functional groups. As a result the polymer composition in such systems can be significantly different from that of pure fluorocarbon chemistries. We account for this possibility in our model by including a hydrogenated polymer species. This species has a reaction hierarchy similar to the fluorocarbon polymer, except for the probability and the threshold energy of the physical sputtering reaction.

Etching of Si is similar to SiO_2 in that it proceeds through the formation of a steady-state polymer layer. The main etch mechanism in Si is fluorination of surface sites by F radicals to progressively form SiF , SiF_2 , and SiF_3 . SiF_x is consumed by ion sputtering to release SiF_n and by F atom etching of SiF_3 to release SiF_4 . The fluorocarbon radicals have a sig-

nificant sticking probability to Si surface, even in the absence of ion activation, and the absence of oxygen in the substrate reduces the rate of consumption polymer. As a result the polymer layers are generally thicker during Si etching thereby reducing the rate of delivery of activation energy to the surface and reducing etch rates.

B. Other processes

The rate of surface kinetics in part depends on the stress of the film.³⁸ This effect is potentially important during plasma etching in the context of notch formation at the interface between, for example, p -Si and SiO_2 . Chang and Sawin showed that tensile stress increased the rate of etching reactions at the interface between p -Si and SiO_2 while compressive stress slowed the rate.³⁹ Porous materials in large part have compressive stress at the inner surfaces of pores with there being more stress with smaller pores. Although stress dependent reaction probabilities are not included in this work, systematic variations of mass corrected etch rates with pore size could be influenced by these effects.

IV. VALIDATION OF THE REACTION MECHANISM FOR SOLID Si AND SiO_2

The reaction mechanism was calibrated and validated for blanket etching of SiO_2 and Si in C_2F_6 , C_4F_8 , and CHF_3 chemistries. Validation of reaction mechanisms for complex gas mixtures such as C_4F_8 –Ar– O_2 will be discussed elsewhere. The cylindrical inductively coupled plasma (ICP) reactor used for this study, shown in Fig. 2, is patterned after that used by Schaepkens *et al.*²⁶ Inductive power is supplied through a 3-turn coil, 16 cm in diameter. The coil sits on a 2 cm thick quartz window, which is 23 cm in diameter. The wafer is on a substrate, which can be independently biased, 7 cm below the quartz window. For the base case, the gas flow rate is 40 sccm and the pressure is 6 mTorr. The coil source current is at 13.56 MHz and delivers an inductive power of

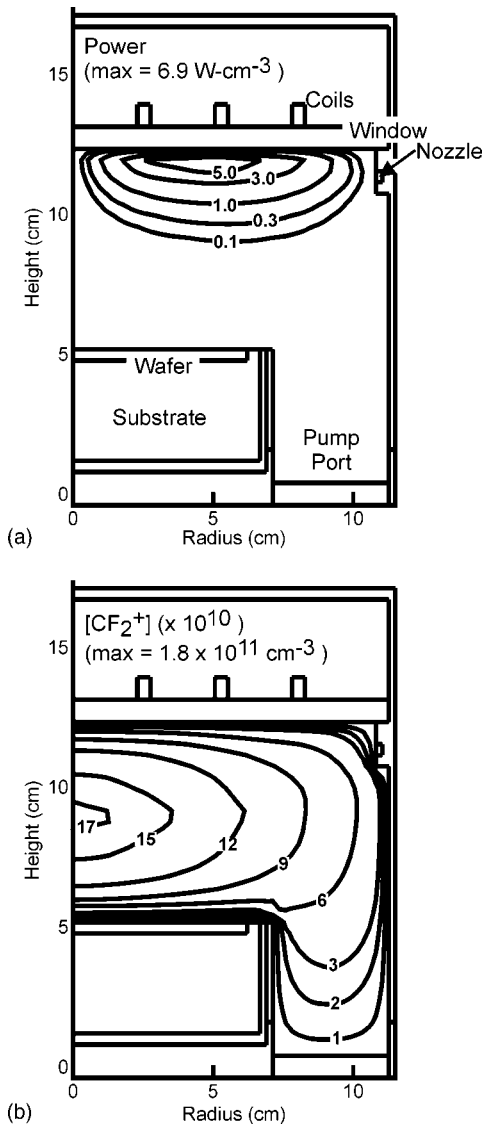


FIG. 2. Plasma properties for the base case (C_2F_6 , 1400 W ICP power, 6 mTorr, 40 sccm) and -110 V self-bias. (a) Power and (b) CF_2^+ density. For these conditions, the plasma is highly dissociated.

1400 W. The rf bias voltage was varied to obtain the required dc self-bias for comparison to experiments. The gas-phase reaction mechanism is discussed in detail in Ref. 40. Power deposition and CF_2^+ density in a C_2F_6 plasma are shown in Fig. 2.

Power deposition is restricted to the top of the reactor within the skin depth of the electromagnetic field, which is a few cm. The large electron density ($\approx 10^{11}$ cm $^{-3}$) highly dissociates the C_2F_6 feedstock gases, whose density peaks near the nozzle. As a result of the high degree of dissociation, the major neutral radicals are CF, CF_2 , and F, and the most abundant ions are CF_2^+ , F^+ , and CF_3^+ . As diffusive transport dominates at low pressures, CF_2 and CF_2^+ densities are larger near the center of the reactor. Due to large rates of recombination of CF_2^+ at the walls the CF_2 density increases near the walls of the reactor.

Radical and ion fluxes to the wafer for the base case con-

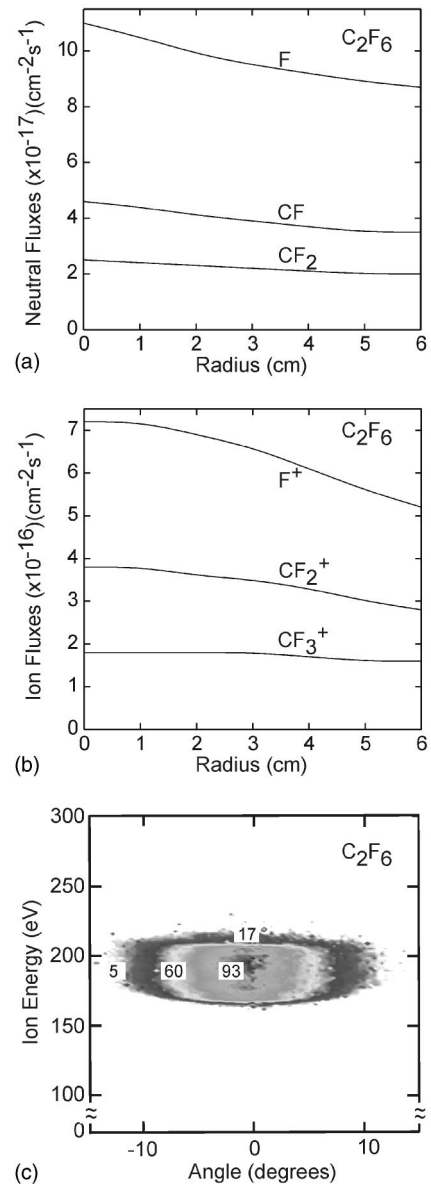


FIG. 3. Fluxes to the surface as a function of radius for the base case conditions for a C_2F_6 plasma. (a) CF_2 , CF, and F. (b) F^+ , CF_2^+ , and CF_3^+ and (c) total ion angular and energy distribution averaged over the wafer. Decreasing polymerizing flux with radius is compensated by decreased physical sputtering and delivery of activation energy by the ions.

ditions for a C_2F_6 plasma are shown in Fig. 3. Lower F atom and ion fluxes may result in thicker passivation layer near the edge of the wafer. In contrast, decreasing polymerizing neutral fluxes may result in thinner polymer near the edges. The net result of the two opposing effects is that the etch rates near the edge of the wafer were slightly lower than at the center. The total ion energy distribution for these conditions is shown in Fig. 3(c). The ions have a fairly narrow spread in energy with a peak near 200 eV. The distribution is representative of the more abundant ions, namely CF_2^+ , CF_3^+ , and F^+ . The angular spread of the distribution is $<10^\circ$.

Etch rates as a function of self-bias for blanket etching of SiO_2 and Si in a C_2F_6 plasma compared to experiments for the base case conditions are shown in Fig. 4(a).²⁶ The onset

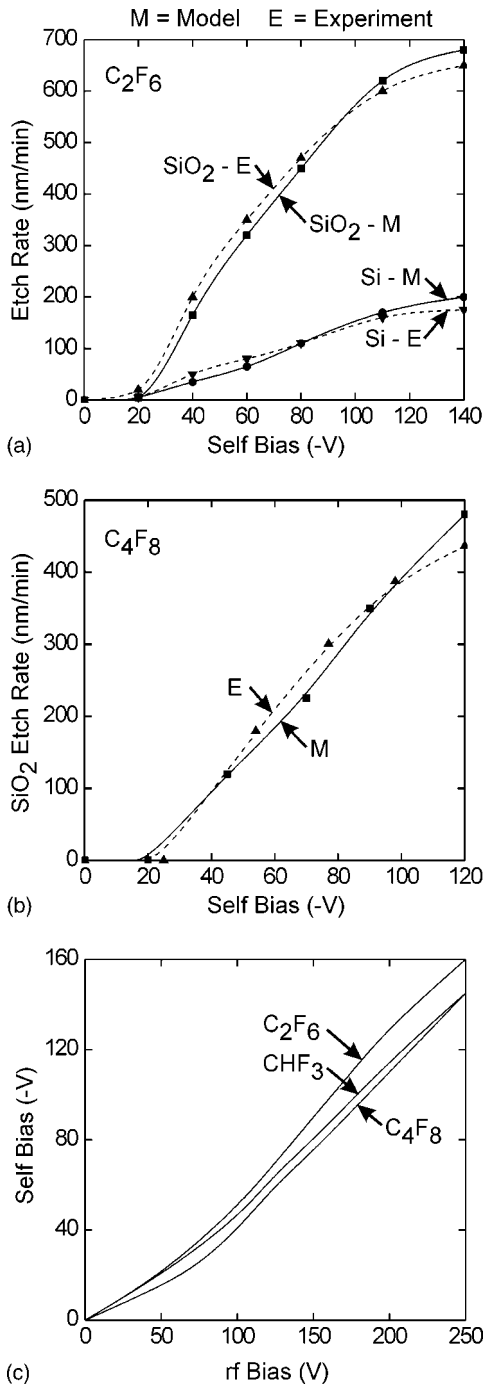


FIG. 4. Comparison of computed and experimental etch rates for SiO₂ and Si as a function of self-bias voltage for (a) C₂F₆ plasmas, (b) C₄F₈ plasmas, and (c) relation between the self-generated dc bias and the applied rf bias amplitude. Etch rates increase with self-bias after a threshold and saturate at high biases. Etch rates of Si are lower due to there being thicker polymer layers, which is the source of selectivity. Experimental results are from Refs. 25 and 26.

of the etching of SiO₂ occurs at -20 V self bias. At low biases and low ion energies, the polymer thickness is large (several nm) due to ion-activated polymer deposition, which is most efficient at low energies. There is also only nominal ion sputtering of the polymer at low energies. (For reference, self generated dc bias voltages as a function of the applied rf

bias amplitude for these conditions are shown in Fig. 4(c). The relationship between the self-bias and rf bias is fairly linear for all the chemistries.) The onset of etching at -20 V self bias occurs when the polymer is thin enough to allow the delivery of activation energy to the polymer-SiO₂ interface, which initiates the etching reaction releasing volatile etch products like CO₂, COF_x, and SiF_x. The etch rate increases with self-bias which corresponds to a monotonic decrease in the polymer thickness due to less ion activation of the polymer precursor and more sputtering. At high self-bias and ion energies, the polymer reduces to sub monolayer thickness leading to insufficient passivation and the etch rate saturates. Similar trends occur for etching of SiO₂ in C₄F₈, also shown in Fig. 4.²⁵ Process conditions in this case are 10 mTorr, 50 sccm, and 1400 W ICP at 13.56 MHz.

The deposition of polymer on Si is rapid due to the lack of polymer-wafer interactions such as those between CF_x in polymer with O in SiO₂. A thicker polymer layer also lowers the delivery of activation energy to the underlying Si. The net result is that the etch rates of Si are typically lower than those of SiO₂. However, the variation of etch rate with respect to self-bias for Si etching is similar to that of SiO₂ etching.

The thickness of the polymer is critical to determining etch rates and threshold biases. Polymer formation, assisted by low energy ions, and polymer consumption processes (ion assisted reaction at the solid interface and polymer sputtering), promoted by high-energy ions, simultaneously govern the passivation layer thickness. The threshold bias for etching qualitatively delineates the energy of ions below which ion-assisted polymer formation dominates and above which ion-assisted activation at the interface or sputtering dominates. Since the behavior of etch rates as a function of bias voltage is a sensitive function of threshold energy (E_t) for ion-activated reactions at the interface, this value was calibrated across all three chemistries (CHF₃, C₂F₆, and C₄F₈). An example of the calibration process is shown in Fig. 5, where the etch rate is shown as a function of self-bias for different values of E_t for C₂F₆ at 6 mTorr. The average ion energy is roughly V_{dc} , however, the range of ion energies extend to as large as $V_{dc} + V_{rf}$. As E_t decreases a larger proportion of the ion energy distribution extends above the activation energy, thereby reducing the bias voltage at which etching begins. At high biases, where significant fractions of ions have energies above the activation energy, increasing E_t had little effect on the etch rate. Based on these results, and similar parameterizations for C₄F₈ and CHF₃, we chose $E_t = 70$ eV.

Polymer growth is initiated at the SiO₂ surface through activation by low energy ions. After the first layer of polymer is formed, the neutral fluorocarbon radicals deposit on the existing polymer layer, thereby increasing the polymer thickness. As the thickness of the polymer critically depends on the rate of incorporation, the sticking probability of fluorocarbon radicals on polymer was also calibrated across the three chemistries. An example of this parameterization is shown in Fig. 5(b). Larger p_0 for fluorocarbon sticking in-

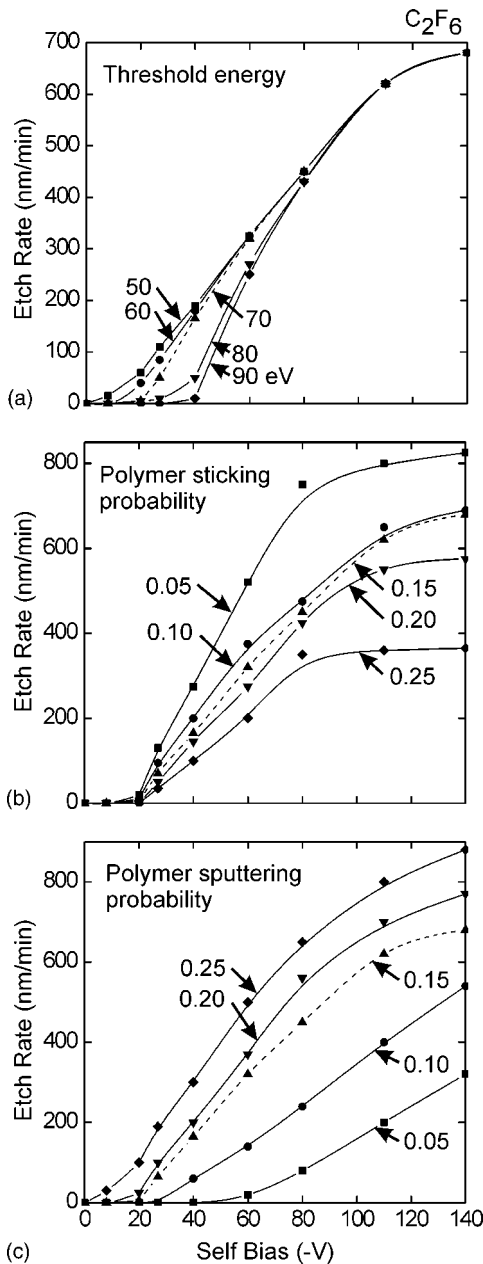


FIG. 5. Sensitivity of reaction parameters for etching of SiO_2 in C_2F_6 plasma. (a) Threshold energy of ion activated processes, (b) fluorocarbon radical sticking probability, and (c) polymer sputtering probability. The threshold in self-bias for the onset of etching increased with increasing threshold energies of and decreasing polymer sputtering probability. Higher polymer sticking probability decreased etch rates at high self-biases. The dotted lines indicate the adopted values.

increases the polymer thickness and lowers the etch rates. The significance of this effect increases with substrate bias. Based on these results we chose $p_0 = 0.15$.

The removal of polymer is dominated by ion sputtering. While keeping the threshold energy for sputtering at 70 eV, the reference probability was parameterized for calibration purposes across the three chemistries. An example of this parameterization is shown in Fig. 5(c) for C_2F_6 at 6 mTorr. Lowering the sputtering probability leads to a thicker polymer layer, which would require a larger fraction of ions

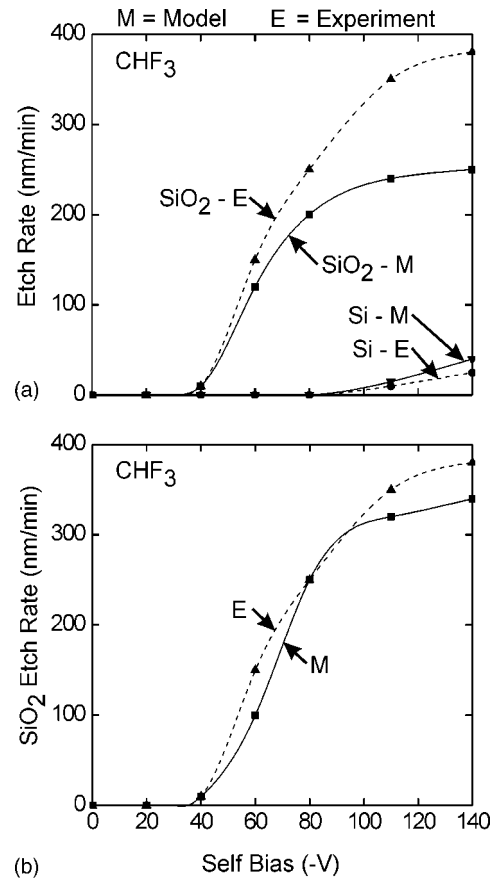


FIG. 6. Comparison of computed and experimental etch rates of SiO_2 and Si as a function of self-bias voltage for CHF_3 plasmas. (a) Without accounting for H radicals in the reaction mechanism. (b) With a hydrogenated polymer species. H radicals cross link to the polymer and change the polymer composition, which are accounted for by modifying polymer sputtering rates. Experimental results are from Ref. 26.

above E_t for etching to proceed. This pushes the onset of etching to higher bias voltages. Even at high biases the polymer thickness is large enough that the etch rates do not saturate with low sputtering probabilities. Based on these results, we chose $p_0 = 0.15$ for polymer sputtering.

Etch rate as a function of self-bias for SiO_2 and Si in a CHF_3 plasma is shown in Fig. 6.²⁶ The process conditions are 6 mTorr, 40 sccm, and 1400 W ICP at 13.56 MHz. Etching of SiO_2 and Si show dissimilar trends. The onset of etching for SiO_2 is -40 V self-bias and for Si is -100 V. Selected radical and ion fluxes to the center of the wafer for the above process conditions for C_2F_6 , C_4F_8 , and CHF_3 chemistries are listed in Table II. The ratio of F fluxes in C_2F_6 to that in CHF_3 is ≈ 3.5 , which results in higher etching of the polymer and lowers the etch rates in C_2F_6 as compared to CHF_3 . In the case of Si etching, since the most prominent etching mechanism is by F atoms, the reduction in the F radical flux has a large effect on the etch rates. As a result there is better selectivity between SiO_2 and Si for CHF_3 .

Note that there is a discrepancy in the etch rates between model and experiments at higher biases. This is likely due to the omission of H radicals from the surface reaction mechanism. The H radicals are able to cross-link to the fluorocar-

TABLE II. Total fluxes of the reactants to the center of the wafer.

Species	Flux ($\text{cm}^{-2} \text{s}^{-1}$)		
	$\text{C}_2\text{F}_6^{\text{a}}$	$\text{C}_4\text{F}_8^{\text{b}}$	CHF_3^{a}
CF_3^+	9.32×10^{15}	5.69×10^{15}	2.78×10^{15}
CF_2^+	1.45×10^{16}	1.34×10^{16}	5.70×10^{15}
F^+	2.88×10^{16}	2.63×10^{16}	1.39×10^{16}
F_2^+	3.16×10^{14}	6.04×10^{14}	6.34×10^{14}
C_2F_4^+	6.68×10^{13}	1.48×10^{15}	2.87×10^{11}
C_2F_3^+	1.85×10^{13}	1.41×10^{13}	7.41×10^{11}
CHF_2^+	1.59×10^{14}
H_2^+	1.17×10^{15}
H^+	8.42×10^{14}
CF_2	2.71×10^{16}	3.85×10^{17}	8.24×10^{15}
CF	2.07×10^{16}	3.26×10^{17}	5.48×10^{15}
F	5.35×10^{16}	5.77×10^{16}	1.56×10^{16}
H	1.15×10^{16}
C_2F_3	9.57×10^{11}	5.51×10^{15}	3.50×10^9
C_2F_4	4.66×10^{12}	2.15×10^{16}	3.91×10^{11}

^a6 mTorr, 40 sccm, 1400 W ICP, -100 V self-bias.

^b10 mTorr, 50 sccm, 1400 W ICP, -110 V self-bias.

bon polymer chains and thus change the polymer composition. This different polymer composition was accounted for in the surface reaction mechanism by treating the hydrogenated polymer as a different species. p_0 and E_t for physical sputtering of hydrogenated polymer were modified to address this difference. E_t was increased to 125 eV and the sputtering probability was increased to 0.28. At low biases, a significant proportion of the ions do not possess the activation energy for the sputtering process. Increasing E_t reduces sputtering and increases the polymer thickness. Increasing the sputtering probability compensates and the net result is that there is no change in the threshold for the onset of etching. However, at high biases, the majority of the ions possess the activation energy for sputtering. Hence increasing E_t to 125 eV has only nominal effect on the polymer layer thickness. As a result at these biases the increased p_0 increases the etch rates and bridges the discrepancies noted earlier. The resulting etch rates as a function of self-bias are shown in Fig. 6(b) and are in better agreement with the experiments.

V. ETCHING OF POROUS SILICA (PS)

A. Validation

To validate the reaction mechanism for PS comparisons were made to experiments for two porous materials ($r_0 = 2$ nm, 30% porosity; and $r_0 = 10$ nm and 58% porosity).²⁵ The Δr_0 (standard deviation of the radius of pore network) was maintained at 50% for r_0 for all cases, unless otherwise specified. Etch rates as a function of self-bias for PS and SS in CHF_3 and C_4F_8 plasmas are shown in Figs. 7 and 8. The process conditions are 10 mTorr, 50, sccm and 1400 W ICP at 13.56 MHz. In general, the etch rate of PS is higher than SS for otherwise the same conditions due to their inherently lower mass densities. This trend is observed for both CHF_3 and C_4F_8 chemistries. The threshold bias for etching and the

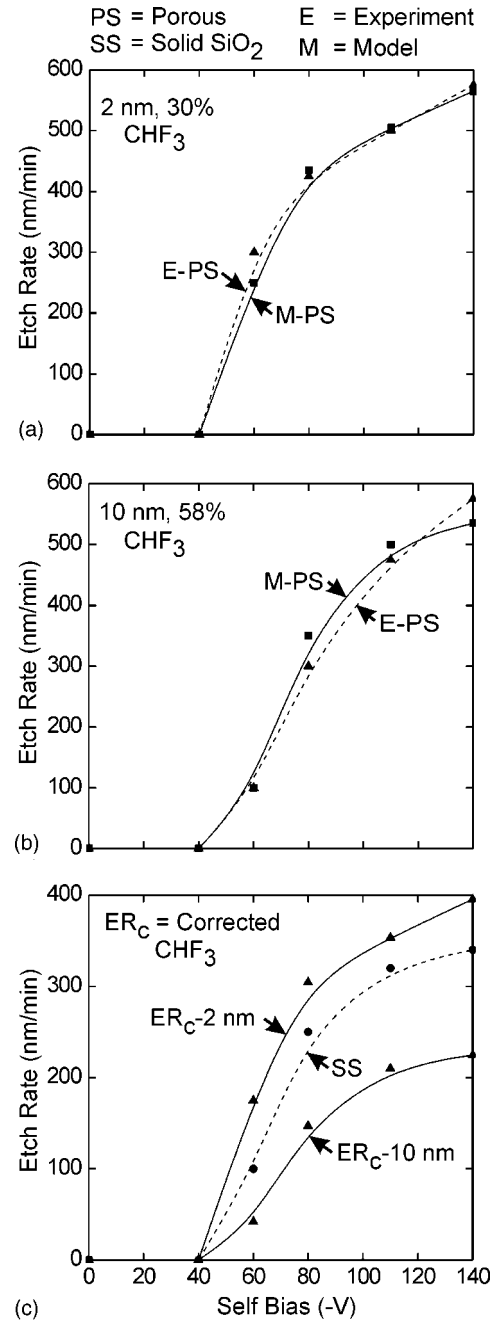


Fig. 7. SS and PS etch rates as a function of self-bias voltage for a CHF_3 plasma for the base case conditions. (a) PS with $r_0 = 2$ nm, 30% porosity, $\Delta r = 1.2$ nm; (b) $r_0 = 10$ nm pore, 58% porosity, $\Delta r = 5$ nm; (c) corrected etch rates. Corrected etch rates are enhanced by small pores and depressed by large pores. These trends also depend on the steady-state polymer thickness. Experimental results are from Ref. 25.

dependence of etch rate on self-bias are similar for PS and SS because of the same governing fundamental reaction chemistry.

To isolate the effects of pores on etch rates, a corrected etch rate (ER_c) is defined as

$$\text{ER}_c = \text{ER}(1 - p), \quad (5)$$

where p is the porosity and ER is the gross etch rate. ER_c is effectively the etch rate per unit mass. If the pore morphol-

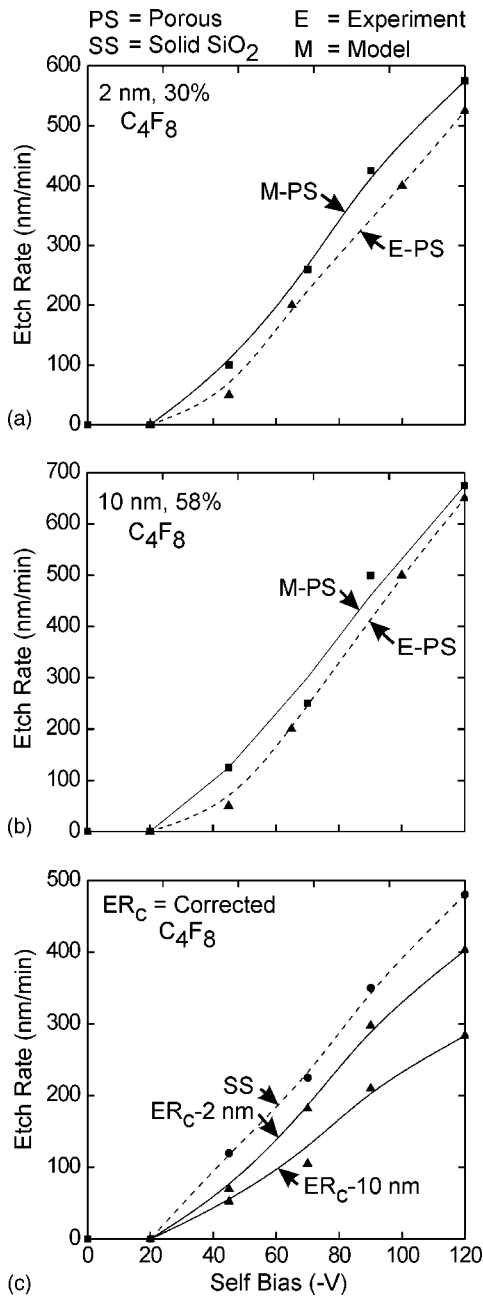


FIG. 8. SS and PS etch rates as a function of self-bias voltage for a C₄F₈ plasma for the base case conditions. (a) PS with $r_0=2$ nm, 30% porosity, $\Delta r=1.2$ nm; (b) $r_0=10$ nm, 58% porosity, $\Delta r=5$ nm; (c) corrected etch rates. Corrected etch rates are depressed by both small and large pores due to a thinner steady state polymer thickness. Experimental results are from Ref. 25.

ogy had no kinetic effect on etching, then the ER_c of PS should be equal to the etch rate of SS. ER_c as a function of self-bias for CHF₃ and C₄F₈ chemistries are shown in Figs. 7(c) and 8(c), respectively. In CHF₃ plasmas, the ER_c of 2 nm PS is larger than that of etch rate of SS and the ER_c of 10 nm PS is smaller than that of SS for all values of self-bias. This result implies that smaller pores enhance the fundamental etch rate in CHF₃ plasmas. However, in C₄F₈, the ER_c of both 2 and 10 nm PS are lower than that of SS, with the ER_c of 10 nm PS being the lowest.

In highly polymerizing environments, a critical parameter, which determines the kinetics of the etching process is the steady-state polymer layer thickness (L). L can vary from a few to many nm, typically 3–8 nm for the chemistries investigated here. This thickness depends on the magnitude and energies of the incident fluxes, which in turn depends on the gas chemistry and process conditions.^{13,25} In the case of PS, as the pores are exposed during etching, they can be filled with polymer. Hence the ratio L/r_0 , where r_0 is the average pore radius, is a significant consideration. For CHF₃ etching of PS with 2 nm pores, L is typically ≈ 5 to 6 nm and greater than r_0 . As a result the increase in the local polymer thickness due to pore filling is fractionally small compared to L . Hence pore filling does not lower the ER_c of PS in comparison to the etch rate of SS. Any enhancements are likely physicochemical effects.

During the etching of blanket SS, the incident ions are, on average, normal to the surface; whereas the optimum angle for chemically enhanced sputtering is $\approx 60^\circ$. When small pores are filled they do not significantly add to the polymer thickness. However, they do present non-normal surfaces to the plasma, which enable more rapid chemically enhanced sputtering. The activation of the polymer–wafer surface is, therefore, likely to be faster, which produces larger etch rates. The difference in the ER_c of PS and etch rate of SS at the threshold self-bias of -40 V is marginal ($<10\%$). With an increase in ion energies, this difference increases to as much as 50%. Larger stresses with smaller pores could also contribute to the enhanced etch rate.³⁹

In the case of C₄F₈ plasmas, L is ≈ 3 to 4 nm and comparable to r_0 for 2 nm pores and so on a fractional basis there is a larger increase in the local polymer thickness. The pore filling effect in this case is large enough to negate the possible enhancement due to perhaps more optimal chemically enhanced sputtering and results in a slightly lower ER_c. In this case the difference in the ER_c of PS and etch rate of solid SiO₂ remains fairly uniform at about 50 nm/min.

With 10 nm pores, L is smaller than r_0 for both CHF₃ and C₄F₈ plasmas. As the pores are opened up by the etching process, they are filled with polymer resulting in the local polymer thickness on top of the SiO₂ bounding the pore being significantly larger than L . This results in a lower delivery of activation energy to the polymer–SiO₂ interface and a slower rate of etching. Larger open pores also tend to have polymer–SiO₂ interfaces exposed to the ion flux at shallower angles, which is less optimum for activating etch processes. A significant proportion of flux reaching interfaces at other sites on the surface of pores consists of reflected neutrals with energies lower than the incident ion flux. The net result of these effects is that the ER_c of 10 nm PS is lower ($\approx 40\%$ – 50%) than the etch rate of SS for both CHF₃ and C₄F₈ chemistries.

B. Effects of porosity and interconnectivity

Computed ER_c and etch rate as a function of porosity for 2 and 10 nm PS etched using a CHF₃ chemistry are shown in Fig. 9. The process conditions are the base case with a self-

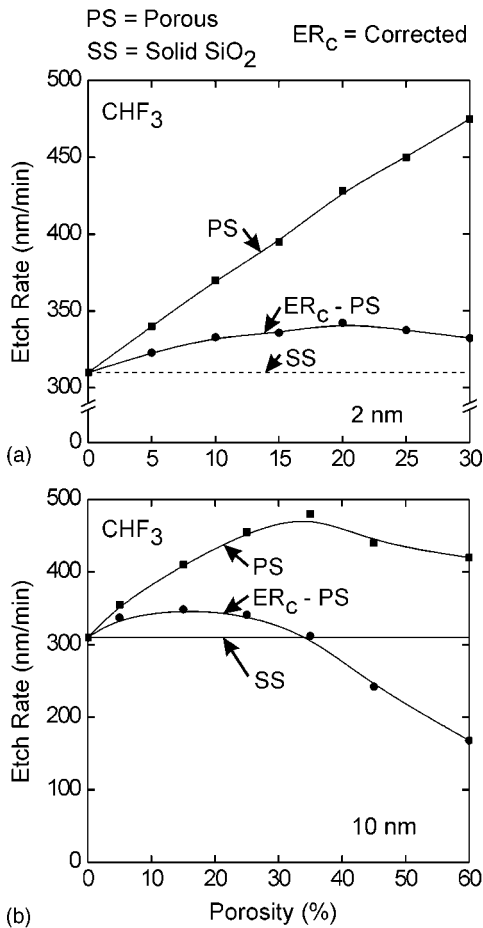


FIG. 9. SS and PS etch rates as a function of porosity for a CHF₃ plasma for the base case conditions. (a) PS with $r_0 = 2$ nm, 30% porosity, $\Delta r = 1.2$ nm; (b) $r_0 = 10$ nm, 58% porosity, $\Delta r = 5$ nm. Etch rate enhancements for small pores are pronounced at higher porosities. Pore filling is more detrimental to etching for large pores at high porosities.

bias of -65 V. As porosity increases with 2 nm pores, there is an increase in the total area of the polymer–SiO₂ interface, which results in increased rates of activation at the interface due to chemically enhanced sputtering. As a consequence the ER_c increases until a porosity of $\approx 25\%$. As the porosity increases further, the cumulative effect of an increased polymer thickness over a larger number of local pores increases the pore filling effect. This causes the ER_c to saturate. For the 10 nm PS, enhancement in the ER_c is obtained only at low porosities ($\leq 15\%$). The pore filling effect eventually dominates and causes the ER_c to fall below the etch rate of SS at a porosity of $\approx 35\%$ at which time the gross etch rate is maximum. The presence of polymer in pores at locations which have no direct view angle to the plasma and so have low sputtering rates exacerbates this effect. In general large r_0 and larger porosities produce an ER_c which may be smaller than SS.

Etch rates as a function of the PS interconnectivity (10 nm, 60%; and 15 nm, 60%) for the base case conditions and self-bias voltages of -65 and -110 V in a CHF₃ plasma are shown in Fig. 10. Since the total porosity remains the same, ER_c is directly proportional to etch rate. In an interconnected

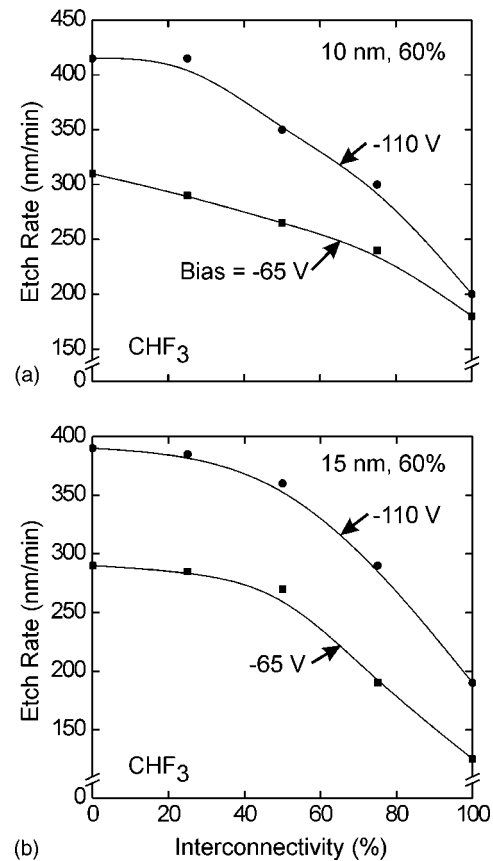


FIG. 10. SS and PS etch rates as a function of pore interconnectivity for a CHF₃ plasma for the base case conditions for self-biases of -65 and -110 V. (a) PS with $r_0 = 10$ nm, 60% porosity, $\Delta r = 5$ nm; (b) $r_0 = 15$ nm, 60% porosity, $\Delta r = 7.5$ nm. Pore filling reduces etch rates at higher pore interconnectivities.

network, adjacent pores are linked to form a chain with a low fractal dimension as opposed to forming a larger pore. As a result when one pore opens up during etching, the entire pore chain is exposed to the plasma. As interconnectivity increases, the average length of the opened pore chains increases. Neutral radicals which are polymer precursors can diffuse deep into the interconnected pores. Since polymer formation is a low energy assisted process, reflected low energy neutrals, which can penetrate into the pore chains, are able to activate polymer formation even though they have no direct line-of sight to the incident flux. However, the reflected neutrals do not deliver sufficient activation energy within the pore chains to either activate etching at the polymer–wafer interface or to sputter the polymer. This leads to polymer build-up, sometimes deep within the network which leads to lower etch rates at high interconnectivity.

VI. PROFILE EVOLUTION OF PS ETCHING IN CHF₃ PLASMAS

A frequent challenge during microelectronic fabrication is the need to etch vias or trenches having high aspect ratios and vertical sidewalls. The goals are often difficult to achieve due to the complex surface reactions on the sidewalls and

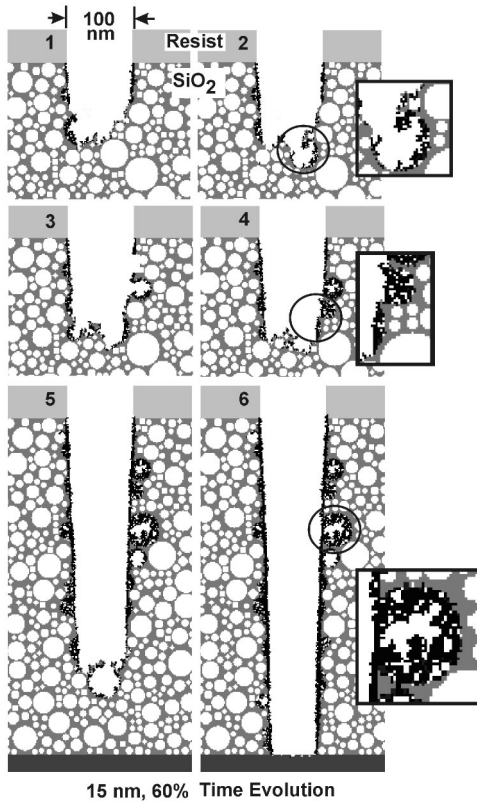


FIG. 11. Time sequence of etch profiles for PS having a closed pore network with $r_0 = 15$ nm, 60% porosity and $\Delta r = 7.5$ nm. The aspect ratio is 5 and Si is the underlying material. The black shading represents polymer. Expanded views of selected outlined portions of the profile are shown in the adjacent boxes. The sequence captures pore breakthrough, polymer filling in the vertical and lateral directions. Pore filling slows the etch process but has little effect on the taper for these conditions.

bottom of the trench. In the case of etching of PS, this is even a more difficult goal to meet due to the complex morphology of the porous and interconnected structures. The challenges of using PS do not stop with the etching of the via or trench but also extends to the subsequent processing of the vias such as cleaning of the residual polymer.

The time evolution of a high aspect ratio feature in a 15 nm, 60% porosity and 0% interconnectivity PS film etched in a CHF_3 plasma for base case conditions (with a self-bias of -65 V) is shown in Fig. 11. The underlying material is Si. The width of the trench is 100 nm and the aspect ratio is 5. The opening of pores, their filling with polymer and the subsequent etching of the filled pore occurs sequentially as the profile evolves. The filling of pores slows down the etching in the vertical direction due to the thicker effective polymer layers. However, the filling of pores or lining of pores with polymer on the sidewalls does not cause any additional tapering of the profile. The etch slows or stops on the underlying Si where the polymer layer is thicker. The tapering of the profile is a result of the sidewall passivation, which stops lateral etching, and is more dependent on the process conditions than on the pore morphology. Although the filling of the side pores does not significantly change the taper of the final etched via, it does create a problem in the subsequent

removal of the polymer. The presence of pores on the sidewalls leads to a jagged topology of the etched via, which is more pronounced for larger radii. This could present challenges for the later deposition of barrier coatings or seed layers.

A. Effects of porosity, pore radius and interconnectivity

Etch depths and corrected etch depths after equal etch times as function of porosity for high aspect ratio trenches for different average pore radii ($r_0 = 4, 10,$ and 16 nm) are shown in Fig. 12. In agreement with earlier observations for blanket etching, smaller pore radii enhance the rate of etching. This effect is more pronounced as the porosity increases due to there being a larger surface area for more favorable angles of incidence of the ions. However, as the pore radius increases, pore filling starts to dominate and the ER_c decreases. For 10 nm PS, the maxima in ER_c is at $\approx 20\%$ porosity and the ER_c decreases below the etch rate of SS at $\approx 50\%$ porosity. Larger pores (15 nm) for which filling is even more critical shows little if any enhancement. The maximum in ER_c occurs at $\approx 10\%$ porosity and the ER_c is smaller than the etch rate of SS for porosities $> 30\%$.

Etch depths and corrected etch depths for high aspect ratio trenches after equal etch times as a function of pore radius are shown in Fig. 13. The 50% porosity material is etched in a CHF_3 plasma. Profiles of the trenches are also shown with Si as the underlying material. The process conditions are the base case with a self-bias of -65 V. As the pore radii increase, L/r_0 decreases. This produces an increase in pore filling, and so the gross etch rate and ER_c uniformly decrease. The final tapers for the different pore radii are quantitatively similar, supporting the earlier observation that the average pore radius and porosity have little effect on the taper of the profile, at least not in any systematic manner. However, the etched vias with larger pores have a more jagged topology and are likely harder to clean.

Etch depth and taper after equal etch times and profiles as function of interconnectivity for 10 nm, 60% PS etched in a CHF_3 plasma are shown in Fig. 14. The taper is given by the ratio W_b/W_t where W_b is the width of the taper 400 nm above the bottom of the trench and $W_t = 100$ nm is the width at the top of the trench. Although the pore radius and porosity have little effect on the taper of the profile, higher interconnectivity decreases the taper. From a near vertical profile for a closed pore network, the profile gradually bows with increasing interconnectivity. The presence of interconnected paths open up more surface area for etching to proceed, which despite the pore filling leads to some bowing. The downside is that polymer can be found deep within the pore network. In accordance with earlier observations for blanket etching, the etch depth decreases with increase in interconnectivity due to polymer build up.

B. Consequences of process conditions

The critical dimensions of the etched profiles depend on the incident magnitudes and energies of the reactant fluxes.

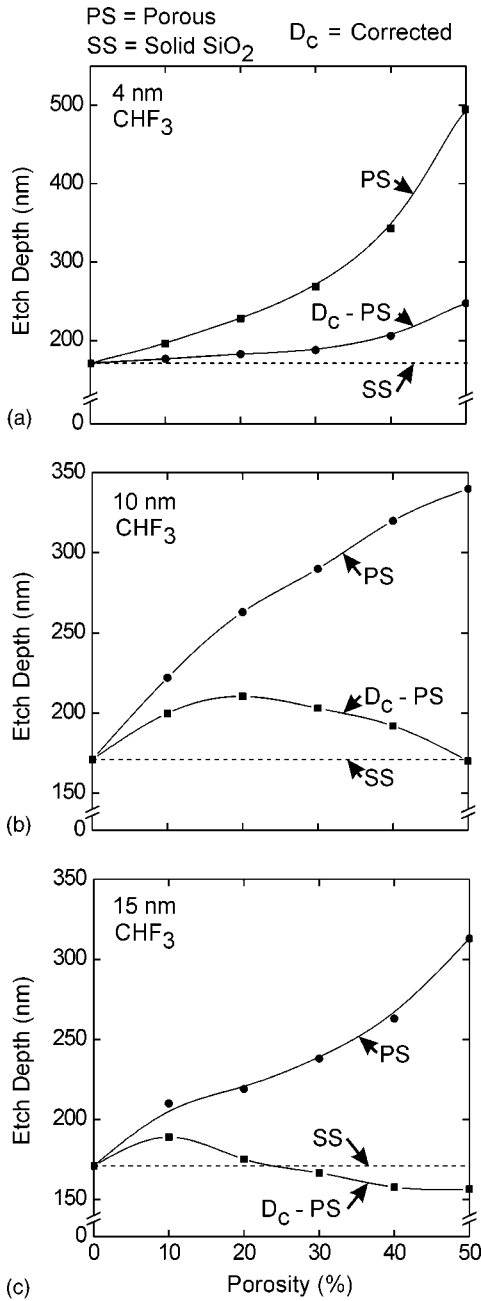


FIG. 12. Etch rates of PS as a function of porosity for etching of high aspect ratio features in a CHF₃ plasma for base case conditions for (a) $r_0=4$ nm, $\Delta r=2$ nm, (b) $r_0=10$ nm, $\Delta r=5$ nm, and (c) $r_0=15$ nm, $\Delta r=7.5$ nm. Pore filling depresses etch rates at progressively lower porosities as the average pore radius increases.

With porous substrates, the pore filling effect might be expected to be sensitive to changes in the incident fluxes and process conditions. To this end, the ratio of the incident polymerizing flux to the ion flux Φ_n/Φ_{ion} , was artificially varied to investigate the effect of the composition of the incident flux on etch characteristics. The gross etch rate, ER_c and taper of PS (2 nm, 30%; and 10 nm, 58%) and SS as a function of Φ_n/Φ_{ion} for etching in a CHF₃ plasma are shown in Fig. 15. ($\Phi_n/\Phi_{ion}=0.4$ corresponds to the base case with a self-bias of -110 V, but otherwise the flux ratios do

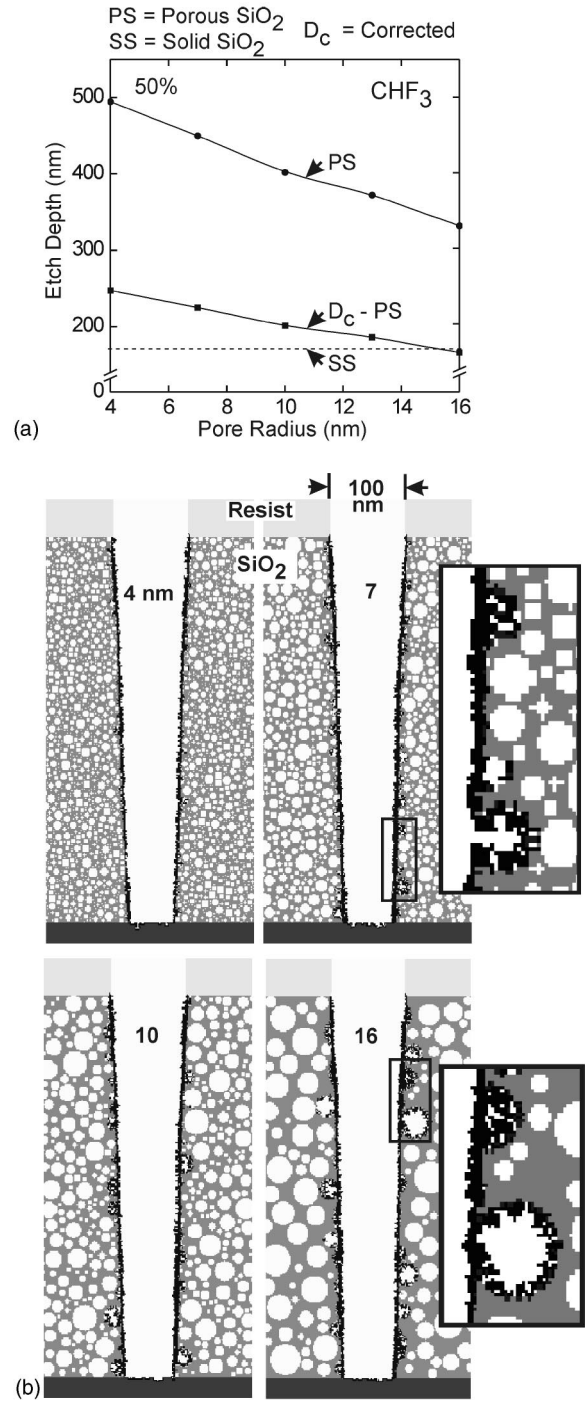


FIG. 13. Etch properties of 50% porosity PS as a function of pore radius for high aspect ratio features in a CHF₃ plasma for the base case conditions. Si is the underlying material. (a) Etch rates. (b) Etch profiles. The black shading represents polymer. Expanded views of selected outlined portions of the profile are shown in the adjacent boxes. The etch rates and corrected etch rates decrease linearly with increasing pore radius. Profiles indicate little dependence of taper with pore radius.

correspond to any particular set of process conditions.) Profiles of high aspect ratio trenches of SS and PS (10 nm, 58%) for the same conditions are shown in Fig. 16 with Si as the underlying material. The sidewall passivation generally increases with increasing Φ_n/Φ_{ion} due to the larger flux of the

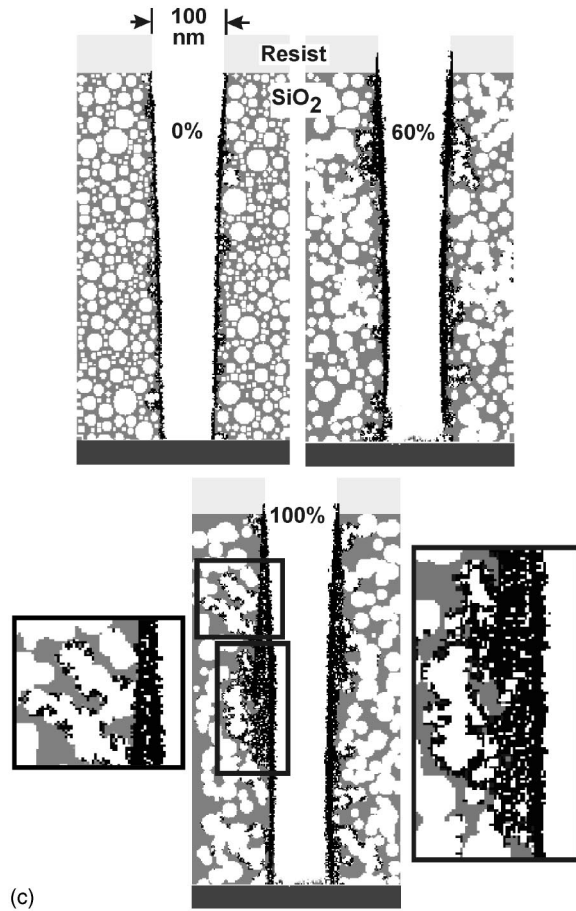
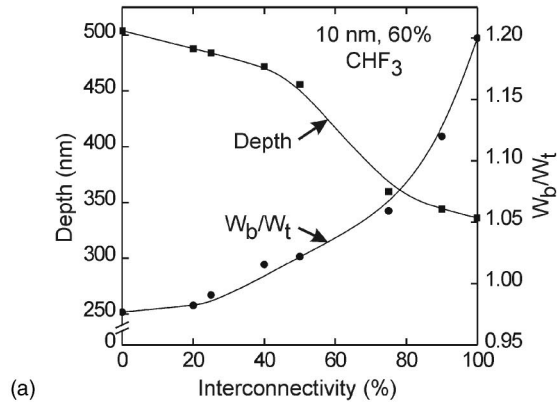


FIG. 14. Effect of interconnectivity on etch properties for etching of high aspect ratio PS features with $r_0=10$ nm, 60% porosity in CHF_3 plasma for the base case. Si is the underlying material. (a) Etch rate and taper. (b) Etch profiles. The black shading represents polymer. Expanded views of selected outlined portions of the profile are shown in the adjacent boxes. Increasing interconnectivity decreases etch rates due to pore filling. Larger interconnectivities produce bowed profiles.

polymerizing radicals. This results in lower rates of etching and produces a narrower profile. An increase in Φ_n/Φ_{ion} also produces thicker polymer layers on the bottom of the trench, which slows the rate of etching. At low values of Φ_n/Φ_{ion} there is insufficient passivation on the bottom of the trench, such that the polymer thickness approaches and broaches a monolayer, and the etch rates are lower. As a consequence

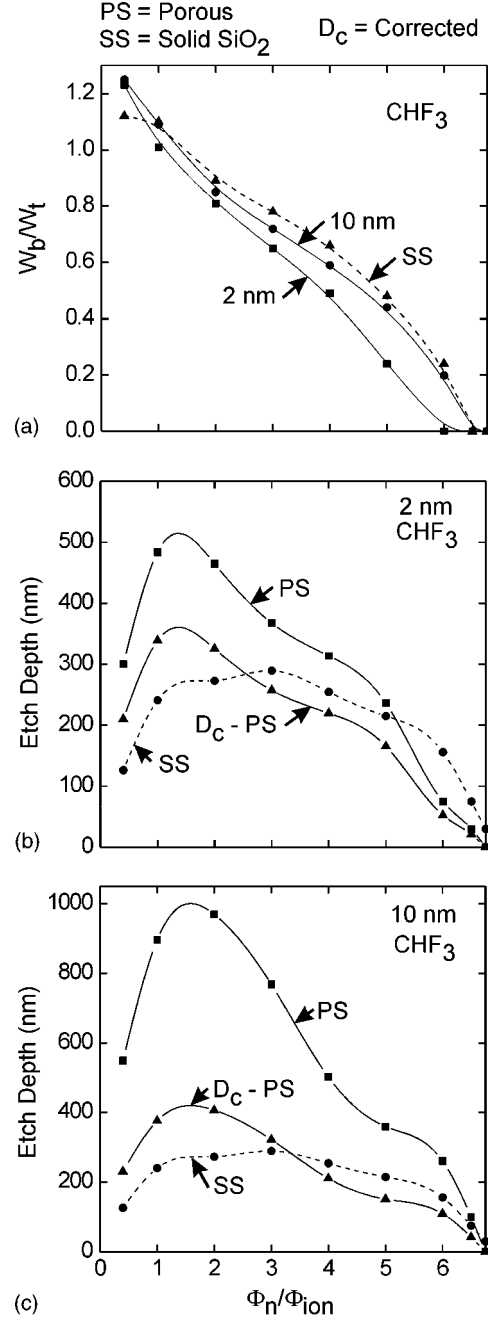


FIG. 15. Influence of passivating neutral to ion flux ratio Φ_n/Φ_{ion} on PS features etched in CHF_3 plasmas for the base case and self bias of -110 V. (a) Taper for PS with $r_0=2$ nm, 30% porosity and $r_0=10$ nm, 58% porosity. (b) Etch depth for PS with $r_0=2$ nm, 30% porosity. (c) Etch depth for PS with $r_0=10$ nm, 58% porosity. D_c is the corrected etch depth. Pore filling increases disproportionately with increasing Φ_n/Φ_{ion} , which reduces the gross etch rate of PS below that of SS.

there is a maximum for the etch rate of SS at $\Phi_n/\Phi_{ion} \approx 2.5$. Etch stop occurs at large values of Φ_n/Φ_{ion} with highly pinched tapers.

ER and taper of PS follow similar trends with respect to Φ_n/Φ_{ion} . As the polymerizing flux increases, pore filling increases and the ER_c of PS decreases below the etch rate of SS at $\Phi_n/\Phi_{ion} \approx 3$. However, with an increase in the polymerizing flux, pore filling increases disproportionately as

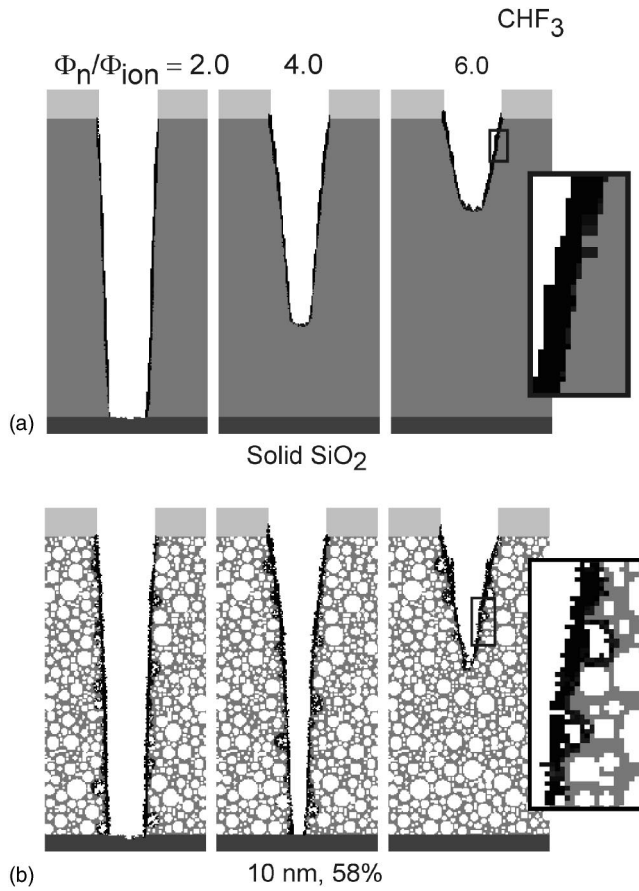


FIG. 16. Profiles of high aspect ratio trenches of SS and PS ($r_0=10$ nm, 60% porosity) etched in a CHF_3 plasma for the base case and self-bias of -110 V as a function of Φ_n/Φ_{ion} . Si is the underlying material. (a) Solid SiO_2 and (b) porous SiO_2 . The black shading represents polymer. Expanded views of selected outlined portions of the profile are shown in the adjacent boxes. As Φ_n/Φ_{ion} increases, the taper increases for both SS and PS, eventually producing an etch stop with a pinched profile.

pores are opened, resulting in excessive polymer build-up on the local sites. This leads to a nonlinear increase in the effective polymer layer thickness. As a result, the gross etch rate of the PS decreases below the etch rate of SS at $\Phi_n/\Phi_{\text{ion}} \approx 3$. For the same reasons, cessation of etching in porous materials occurs at somewhat smaller values of Φ_n/Φ_{ion} .

The gross etch rate, ER_c and taper for high aspect ratio trenches as a function of self-bias for base case CHF_3 etching are shown in Fig. 17. An increase in the bias leads to larger average ion energies which reduces the passivation layer thickness on both the sidewalls and the trench bottom. This produces wider features as the profiles transition from tapered to vertical to bowed as the bias is increased. The increase in etch rate with bias saturates at high biases, in accordance with earlier observations for blanket etching.

The scaling with respect to self-bias is qualitatively the same for PS and SS. The saturation of etch rates with bias for PS and SS in high aspect ratio features occurs at lower biases than for blanket etching. This is likely due to the lower average ion and reflected neutral energies at the bottom of the trench due to sidewall scatter. The ER_c for PS increases with

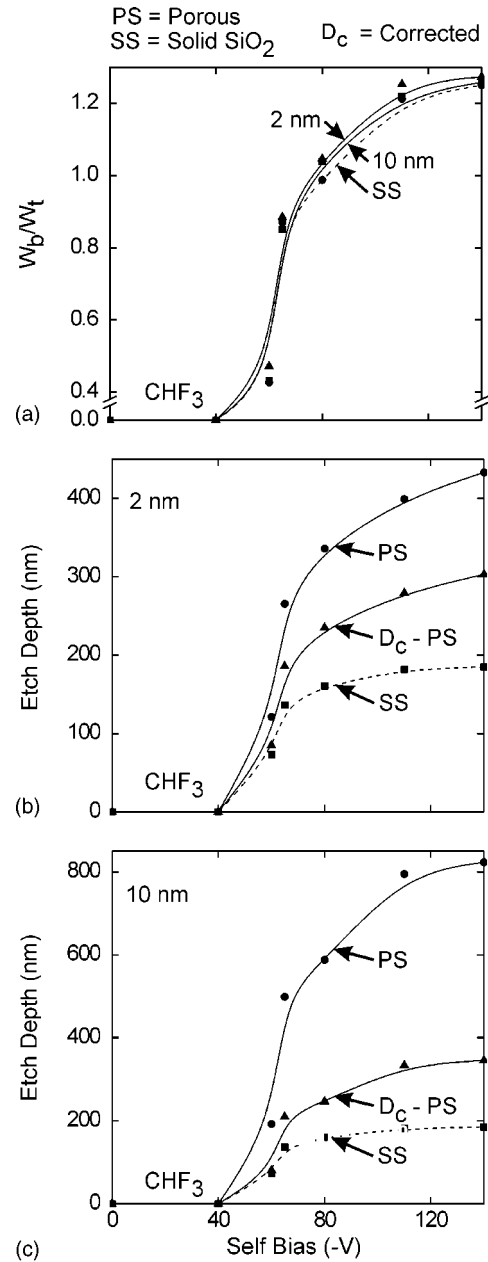


FIG. 17. Properties of PS features etched in CHF_3 plasmas for the base case conditions as a function of self-bias. (a) Taper ($r_0=2$ nm, 30% porosity and $r_0=10$ nm, 58% porosity), (b) etch depth ($r_0=2$ nm, 30% porosity), and (c) etch depth ($r_0=10$ nm, 58% porosity). The increase in reflected neutral energies with increasing bias more acutely affect the PS materials.

respect to SS as the self-bias increases. With a larger bias, the energy of both the ions and their reflected neutrals increases. Reductions in pore filling which increases ER_c is, to some degree, more sensitive to the reflected neutrals since they are able to reach surfaces with poor view angles to the plasma. As the energies of the reflected neutrals (which, on the average, are always smaller than the directly incident ions) increase, the rate of polymer activation decreases and the rate of polymer sputtering increases. At biases where processes activated by direct ion bombardment have satu-

rated, those activated by reflected species (that is, inside pores) continues to increase.

C. General applicability of trends

The reaction probabilities used in the model, though based on experiments, are derived in part by comparison and calibration to experiments in a limited parameter space. As a result, the general applicability of the model and its results may be questioned. In this regard, perhaps the most general finding of the work is the illumination of the synergy (or lack of synergy) between spatial and energy scales. For example, in etching of features in interconnected PS, there are at least three spatial scales: Feature, pore, and network. The morphology and rate of processing on each scale is determined by the relative contributions of low energy particles (ions and reflected neutrals, and polymerizing radicals) which are precursors for polymerization, and high energy particles which are precursors for polymer removal and etch activation. On the feature scale, high energy particles dominate the kinetics. In all but the most polymerizing environments, the contributions of low energy particles to polymerization can be controlled (or overcome) by increasing bias, and so rates and morphologies are bias driven.

In transitioning from feature scale to pore to network, the disparity in the contributions between low energy and high energy precursors becomes more acute. Even with large biases, high energy particles are unable to penetrate into the small features of the pore networks or access surfaces without view angles to the plasma. As such, low energy particles dominate the kinetics by activating polymerization on these surfaces without there being a regulating high energy counterpart. Highly polymerizing conditions exacerbate these effects by fillings pores and increasing the local polymer thickness, thereby making high energy particles an even more valuable regulating commodity. The repercussions in the disparate contributions of low energy and high energy particles in pores and networks play out during the plasma removal of polymer, as discussed in Part II.³² Given this sensitivity of pores and networks to polymerization, process integration of porous materials may require means of selectivity which are less dependent on polymerization.

VII. CONCLUDING REMARKS

Surface reaction mechanisms for etching of PS and SS in fluorocarbon gas chemistries have been discussed based on results from a computational investigation using a reactor scale model coupled to a feature scale model. The reaction mechanism was validated by comparison to experiments. Fluorocarbon etching proceeds through the formation of a steady-state polymer layer on SiO₂ which regulates the incident flux and delivery of activation energy. Polymer formation is assisted by low energy ions. The polymer layer is consumed by energetic ion sputtering. It is also consumed by chemically enhanced sputtering at the interface which releases the etch products. The steady state polymer thickness determines etch selectivity between different materials and the etch kinetics for different process conditions.

The model has been applied to the investigation of etching of PS for different values of porosity, average pore radius and interconnectivity. Etching of PS and SS were found to obey similar scaling laws. However the mass corrected etch rates may differ from the etch rates of SS depending on the degree of pore filling by polymers and the propensity of chemically enhanced sputtering. For small pores, where $L > r_0$, etch rates are enhanced due to there being a larger proportion of ions striking the surface with near optimal angles and increasing the chemical sputtering. Whereas for $L < r_0$ in larger pores, pore filling reduces the etch rates due to there being a larger effective polymer thickness. This is most significant at high porosities, large average pore radius and high interconnectivities.

Etch rates for high aspect ratio trenches showed dependencies similar to blanket etching. The profiles changed from tapered to bowed with increasing bias and decreasing Φ_n/Φ_{ion} . The pore filling effect was particularly sensitive to increases in polymerizing fluxes. Scaling laws for the taper of the profile for SS are generally applicable to PS. Pore radius and porosity have little effect on the taper of the profile. However, the profile becomes bowed as the porous network becomes more interconnected.

ACKNOWLEDGMENTS

This work was supported by the National Science Foundation (CTS99-74962, CTS03-15353), Semiconductor Research Corporation and Sematech.

- ¹S.-J. Wang, H.-H. Park, and G.-Y. Yeom, *Jpn. J. Appl. Phys., Part 1* **39**, 7007 (2000).
- ²G. S. Oehrlein, T. E. F. M. Standaert, and P. J. Matsuo, in *Solid State Technology; Vol. May 2000* (2000), p. 125.
- ³T. E. F. M. Standaert, P. J. Matsuo, X. Li, G. S. Oehrlein, T. M. Lu, R. Gutmann, C. T. Rosenmayer, J. W. Bartz, J. G. Langan, and W. R. Entley, *J. Vac. Sci. Technol. A* **19**, 435 (2001).
- ⁴D. Fuard, O. Joubert, L. Vallier, and M. Bonvalot, *J. Vac. Sci. Technol. B* **19**, 447 (2001).
- ⁵D. Fuard, O. Joubert, L. Vallier, M. Assous, P. Berruyer, and R. Blanc, *J. Vac. Sci. Technol. B* **19**, 2223 (2001).
- ⁶P. Ho, J. E. Johannes, R. J. Buss, and E. Meeks, *J. Vac. Sci. Technol. A* **19**, 2344 (2001).
- ⁷M. Matsui, F. Uchida, M. Kojima, T. Tokunaga, F. Yano, and M. Hasegawa, *J. Vac. Sci. Technol. A* **20**, 117 (2002).
- ⁸W. D. Gidley, W. E. Frieze, T. L. Dull, J. Sun, A. F. Yee, C. V. Nguyen, and D. Y. Yoon, *Appl. Phys. Lett.* **76**, 1282 (2000).
- ⁹W. Wu, W. E. Wallace, E. K. Lin, G. W. Lynn, C. G. Glinka, T. E. Ryan, and H. Ho, *J. Appl. Phys.* **87**, 1193 (2000).
- ¹⁰M. R. Baklanov, K. P. Mogilnikov, V. G. Polovinkin, and F. N. Dultsev, *J. Vac. Sci. Technol. B* **18**, 1385 (2000).
- ¹¹W. D. Gidley, W. E. Frieze, T. L. Dull, A. F. Yee, T. E. Ryan, and H. Ho, *Phys. Rev. B* **60**, R5157 (1999).
- ¹²M. P. Petkov, M. H. Weber, K. G. Lynn, K. P. Rodbell, and S. A. Cohen, *Appl. Phys. Lett.* **74**, 2146 (1999).
- ¹³T. E. F. M. Standaert, P. J. Matsuo, S. D. Allen, G. S. Oehrlein, and T. J. Dalton, *J. Vac. Sci. Technol. A* **17**, 741 (1999).
- ¹⁴A. J. Bariya, C. W. Frank, and J. P. McVittie, *J. Electrochem. Soc.* **137**, 2575 (1990).
- ¹⁵T. E. F. M. Standaert, M. Schaepekens, N. R. Rueger, P. G. M. Sebel, G. S. Oehrlein, and J. M. Cook, *J. Vac. Sci. Technol. A* **16**, 239 (1998).
- ¹⁶M. Matsui, T. Tatsumi, and M. Sekine, *J. Vac. Sci. Technol. A* **19**, 2089 (2001).
- ¹⁷G. S. Oehrlein and J. F. Rembetski, *IBM J. Res. Dev.* **36**, 140 (1992).

- ¹⁸N. R. Rueger, J. J. Beulens, M. Schaepkens, M. F. Doemling, J. M. Mirza, T. E. F. M. Standaert, and G. S. Oehrlein, *J. Vac. Sci. Technol. A* **15**, 1881 (1997).
- ¹⁹M. Matsui, T. Tatsumi, and M. Sekine, *J. Vac. Sci. Technol. A* **19**, 1282 (2001).
- ²⁰K. Miyata, M. Hori, and T. Goto, *J. Vac. Sci. Technol. A* **15**, 568 (1997).
- ²¹R. J. Hoekstra, M. J. Grapperhaus, and M. J. Kushner, *J. Vac. Sci. Technol. A* **15**, 1913 (1997).
- ²²D. Zhang and M. J. Kushner, *J. Vac. Sci. Technol. A* **19**, 524 (2001).
- ²³J. Lu and M. J. Kushner, *J. Vac. Sci. Technol. A* **19**, 2652 (2001).
- ²⁴R. L. Kinder and M. J. Kushner, *J. Appl. Phys.* **90**, 3699 (2001).
- ²⁵T. E. F. M. Standaert, E. A. Joseph, G. S. Oehrlein, A. Jain, W. N. Gill, P. C. J. Wayner, and J. L. Plawsky, *J. Vac. Sci. Technol. A* **18**, 2742 (2000).
- ²⁶M. Schaepkens, T. E. F. M. Standaert, N. R. Rueger, P. G. M. Sebel, G. S. Oehrlein, and J. M. Cook, *J. Vac. Sci. Technol. A* **17**, 26 (1999).
- ²⁷A. Sankaran and M. J. Kushner, *J. Vac. Sci. Technol. A* **22**, 1260 (2004).
- ²⁸R. L. Kinder and M. J. Kushner, *J. Vac. Sci. Technol. A* **19**, 76 (2001).
- ²⁹R. J. Hoekstra and M. J. Kushner, *J. Vac. Sci. Technol. A* **16**, 3274 (1998).
- ³⁰R. J. Hoekstra and M. J. Kushner, *J. Vac. Sci. Technol. B* **16**, 2102 (1998).
- ³¹A. M. Barklund and H.-O. Blum, *J. Vac. Sci. Technol. A* **10**, 1212 (1992).
- ³²M. Schaepkens, G. S. Oehrlein, C. Hedlund, L. B. Jonsson, and H.-O. Blum, *J. Vac. Sci. Technol. A* **16**, 3281 (1998).
- ³³H. Chae, S. A. Vitale, and H. H. Sawin, *J. Vac. Sci. Technol. A* **21**, 381 (2003).
- ³⁴B. E. E. Kastenmeier, P. J. Matsui, and G. S. Oehrlein, *J. Vac. Sci. Technol. A* **6**, 2047 (1998).
- ³⁵M. Inayoshi, M. Ito, M. Hori, T. Goto, and M. Hiramatsu, *J. Vac. Sci. Technol. A* **16**, 233 (1998).
- ³⁶J. P. Booth, G. Cunge, P. Chabert, and N. Sadeghi, *J. Appl. Phys.* **85**, 3097 (1999).
- ³⁷D. C. Gray, I. Tepermeister, and H. H. Sawin, *J. Vac. Sci. Technol. B* **11**, 1243 (1993).
- ³⁸E. Kobeda and E. A. Irene, *J. Vac. Sci. Technol. B* **7**, 163 (1989).
- ³⁹J. P. Chang and H. H. Sawin, *J. Vac. Sci. Technol. B* **19**, 1870 (2001).
- ⁴⁰A. V. Vasenkov, X. Li, G. S. Oehrlein, and M. J. Kushner, *J. Vac. Sci. Technol. A* **22**, 511 (2004).